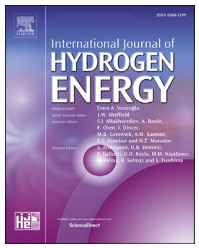
Available online at www.sciencedirect.com

ScienceDirect

journal homepage: www.elsevier.com/locate/he



Strontium iron molybdenum oxide as electrocatalyst for nitrous oxide reduction in solid oxide fuel cells

Laura I.V. Holz [a,b,*], *Francisco J.A. Loureiro* [a,b,**], *Vanessa C.D. Graça* [a,b], *Sergey M. Mikhalev* [a,b], *Celina Fernandes* [c,d], *Adélio Mendes* [c,d], *Duncan P. Fagg* [a,b,***]

[a] *TEMA - Centre for Mechanical Technology and Automation, Department of Mechanical Engineering, University of Aveiro, 3810-193 Aveiro, Portugal*

[b] *LASI - Intelligent Systems Associate Laboratory, Portugal*

[c] *LEPABE, Faculdade de Engenharia, Universidade do Porto, Rua Dr. Roberto Frias, 4200-465 Porto, Portugal*

[d] *ALiCE – Associated Laboratory in Chemical Engineering, Faculty of Engineering, University of Porto, Rua Dr. Roberto Frias, 4200-465 Porto, Portugal*

HIGHLIGHTS

- The viability of SFMO as electrocatalysts for N_2O reduction is demonstrated.
- The N_2O electroreduction mechanism on the SFMO cathode is outlined.
- Competition between O_2 electroreduction and N_2O decomposition is suggested.

ARTICLE INFO

Article history:
Received 17 January 2023
Received in revised form
30 March 2023
Accepted 25 May 2023
Available online 11 June 2023

Keywords:
Solid oxide fuel cell (SOFC)
Strontium iron molybdenum oxide (SFMO)
Nitrous oxide (N_2O)
Oxygen reduction reaction (ORR)
Solid-state electrochemistry

ABSTRACT

Nitrous oxide (N_2O) is an environmentally damaging gas and alternative methods for its abatement are needed. In this work, we developed an electrochemical route using the mixed ionic electronic conductor $Sr_2Fe_{1.5}Mo_{0.5}O_{6-\delta}$ (SFMO) as electrocatalyst for N_2O reduction in the temperature range of 600–800 °C, at ambient pressure, for application in Solid Oxide Fuel Cells (SOFCs). The electrode mechanism, studied by electrochemical impedance spectroscopy (EIS), is discussed to involve a competition between both O_2 and N_2O species, particularly at lower temperatures, where N_2O thermal decomposition is lower. In terms of electrocatalytic properties, galvanostatic transients were used to assess N_2O electroreduction on the SFMO electrode. The results showed that, after cathodic polarization, the N_2O conversion increases. In particular, a highest Faradaic efficiency ($|\Lambda|$) of 3.94 was obtained at 600 °C. The reversibility of the mechanism was also assessed, and the results showed that the reaction rate returns to its open circuit value upon current interruption. This work indicates, therefore, that the electrochemical promotion of N_2O

* *Corresponding author*. TEMA - Centre for Mechanical Technology and Automation, Department of Mechanical Engineering, University of Aveiro, 3810-193 Aveiro, Portugal.
** *Corresponding author*. TEMA - Centre for Mechanical Technology and Automation, Department of Mechanical Engineering, University of Aveiro, 3810-193 Aveiro, Portugal.
*** *Corresponding author*. TEMA - Centre for Mechanical Technology and Automation, Department of Mechanical Engineering, University of Aveiro, 3810-193 Aveiro, Portugal.
E-mail addresses: lauraholz@ua.pt (L.I.V. Holz), francisco.loureiro@ua.pt (F.J.A. Loureiro), duncan@ua.pt (D.P. Fagg).

https://doi.org/10.1016/j.ijhydene.2023.05.251

0360-3199/© 2023 The Authors. Published by Elsevier Ltd on behalf of Hydrogen Energy Publications LLC. This is an open access article under the CC BY license (http://creativecommons.org/licenses/by/4.0/).

reduction can be an attractive tool to be implemented for the reduction of this environmentally damaging gas in SOFC systems.

© 2023 The Authors. Published by Elsevier Ltd on behalf of Hydrogen Energy Publications LLC. This is an open access article under the CC BY license (http://creativecommons.org/licenses/by/4.0/).

Introduction

The European Union's directives aim for a reduction in the emissions of greenhouse gases of 42% by 2030. Among the most problematic greenhouse gases, nitrous oxide (N_2O) stands out as one of the most important one [1]. This gas is responsible for many environmental problems such as ozone layer depletion, global warming [2] and formation of acid rains. The major anthropogenic emissions are associated with diverse human activities, such as nitric and adipic acid production, food production and burning of fossil fuels [3–7].

Selective catalytic reduction is the most common and effective technology to mitigate N_2O, however, it uses some reducing agents as ammonia, hydrogen, and hydrocarbons to reduce this molecule into N_2. Although this process is efficient, it has the drawback of producing carbon dioxide; either directly, during combustion of the hydrocarbons, or indirectly, during synthesis of the reductants, such as H_2 or NH_3 [8]. Conversely, N_2O can also be used to generate electricity by acting as the oxidant in Solid Oxide Fuel Cells (SOFCs), thus, becoming a potential oxidant gas as an alternative for electroreduction in SOFC electrodes [9].

The double perovskite strontium iron molybdenum oxide, $Sr_2Fe_{1.5}Mo_{0.5}O_{6-\delta}$ (SFMO), has gained increasing attention as electrode due to its high structural stability in both reducing and oxidizing atmospheres [10–12], good electronic conductivity and excellent oxide-ion conductivity (~30 S cm^{-1} and 0.13 S cm^{-1} at 800 °C, respectively) [13–16]. The origin of the very high ionic conductivity is predicted from density functional theory (DFT) calculations [17] to be related to the high oxygen vacancy concentration along Fe–O–Fe chains, as well as a low barrier for oxide-ion migration (≈0.3 eV). Interestingly, this activation energy is much lower than those found for traditional ABO_3 perovskite electrode materials (≈0.8/0.9 eV), thus, potentially privileging the SFMO compounds to be used as oxygen electrodes over broader temperature ranges. As a result, the oxygen self-diffusion coefficient, D^*, is around 10^{-6} cm^2 s^{-1} at 750 °C [18], which is comparable with that for LSCF, under similar conditions [19].

The typical formula of a double perovskite oxide is $A_2BB'O_6$, where the A-site cations are larger than the B- and B′-site cations have a similar size of oxygen ions [20]. SFMO has generated interest for use as both anode and cathode for symmetrical cells, due to its good conductivity in oxidizing and reducing conditions, where its electronic conductivity originates due to the coexistence of the mixed-valent Mo^{5+}/Mo^{6+} and Fe^{3+}/Fe^{4+} pairs [13,21]. Goodenough et al. [22] reported that the reason for its redox stability is associated with the fact that even in a reducing atmosphere, the reduction of Fe^{3+} to Fe^{2+} is not complete, due to a band overlapping of Mo^{5+}/Mo^{6+} with Fe^{3+}/Fe^{2+} couple, which protects the ion Fe^{3+} to be completely reduced in the perovskite-type structure. The redox pairs of Fe^{2+} + Mo^{6+} ↔ Fe^{3+} + Mo^{5+} are expected to create electronic carriers, as well as to introduce oxygen vacancies into the lattice that can allow ionic conduction [23], while in oxidizing conditions the electrical charge is mainly balanced by Fe^{4+} and Mo^{6+} and the charge carriers are governed by electronic holes [21,24].

While SFMO has been extensively studied for Solid Oxide Fuel Cell (SOFC) applications [16,20,25,26], electrochemical studies of oxygen cathodes tested in N_2O atmospheres with emphasis in electrocatalysis remain overlooked. Therefore, in the present study, we developed a 3-probe cell reactor, made of 8YSZ electrolyte, SFMO as working electrode and gold (Au) as counter and reference electrodes to study the electrode mechanism of the SFMO electrode in both air and N_2O atmospheres. Aiming to prevent the inter-reaction of YSZ with SFMO, an interlayer made of $Ce_{0.9}Gd_{0.1}O_{2-\delta}$ (CGO10) was used. Moreover, in an unconventional departure, in this work, we attempt to bridge the solid-state chemistry with heterogenous catalysis, with the aim of studying also the non-Faradaic electrochemical modification of catalytic activity (NEMCA) [2] of the N_2O reduction reaction, using SFMO as electrocatalyst.

Experimental

Electrocatalyst preparation

Powders of the $Sr_2Fe_{1.5}Mo_{0.5}O_{6-\delta}$ (SFMO) composition were produced by the sol-gel method. Stoichiometric amounts of Sr, Fe nitrates and $(NH_4)_6Mo_7O_{24}$ were dissolved in distilled water. Ethylenediaminetetraaceticacid (EDTA) was later used as a gelatin agent at 90 °C, forming black precursors. The resultant powder was calcined at 600 °C (heating/cooling rate of 3 °C min^{-1}, dwell time of 4 h). The calcined powder was pressed and calcined at 1200 °C during 10 h.

For the synthesis of $Ce_{0.9}Gd_{0.1}O_{2-\delta}$ (CGO) powder, the combustion method was used. Firstly, the corresponding nitrates in stoichiometric ration were dissolved in distilled water at 90 °C. Citric acid was then added with the aim of promoting the combustion reaction at 150 °C. Finally, to obtain pure phase, the resultant powder was calcined at 1150 °C during 5 h. The CGO powder was then milled at 350 rpm during 5 h.

X-ray diffraction (XRD) was performed to structurally characterize the materials of this work, using a *Rigaku SmartLab* diffractometer (Cu Kα radiation – 1.5406 Å, 40 kV, 30 mA). The patterns were obtained in the range of $20° < 2\theta < 80°$, scan speed of 3° min^{-1}. *Rietveld* refinement was performed using the *SmartlabStudio* software. A pseudo-Voigt peak profile function was used for the profile fitting and the background

was fitted with a B-spline function. For grazing incidence measurements (GIXD), the patterns were collected for different incident angles (0.25, 0.5, 1, 2, 5, and 8°) using a scan speed of 0.6° min^{-1}.

Thermogravimetric (TG) experiments (*NETZSCH TG 209*) were performed by heating the powder under synthetic air at 1150 °C, heating rate of 5 °C min^{-1}, dwell time of 1 h.

Fabrication of the 3-probe cell

For the fabrication of the electrolyte substrates, powders of 8YSZ ($(ZrO_2)_{0.92}(Y_2O_3)_{0.08}$ from TOSOH) composition were uniaxially pressed and sintered at 1600 °C during 10 h with a heating rate of 4 °C min^{-1} and cooling rate of 2 °C min^{-1}. A thing CGO buffer layer was fabricated using spin coating, where the prepared suspension (more detailed information can be found elsewhere [27]) was deposited on the top of 8YSZ, followed by sintering at 1350 °C in air. The SFMO ink was prepared by mixing the powder with a solution of 95 wt% of terpineol + 5 wt% of ethyl cellulose in a 20:80 vol% (powder:-solution) ratio. To this mixture, 3 wt% of stearic acid was added as dispersant and milled in an agate mortar for 15 min. The resultant slurry was then screen-printed on the top of the CGO buffer layer and thermally treated at 350 °C for 1 h to remove the organic binders, followed by sintering at 1000 °C for 4 h in air (with heating/cooling rate 1.5 °C min^{-1}). The final area of the working electrode was 0.2 cm^2. For a 3-probe cell arrangement, while the SFMO was the working electrode, gold (Au) was applied as both counter and reference electrodes to avoid additional catalytic activity, Fig. 1. Here, the Au counter electrode was brush-painted symmetrically to the working electrode and the Au reference electrode was applied as a ring at the edge of the electrolyte substrate [28].

The microstructure of the cell was observed by in a fractured cross-section of the sample by Scanning Electron Microscopy (SEM), *Hitachi TM4000 plus*. The microscope was operated using an applied voltage of 15 kV, using a Backscattered Electron (BSE) detector. Grazing incidence X-ray diffraction (GIXD) was performed to examine potential phase interreactions between the different layers of the 3-probe cell, using a Rigaku SmartLab diffractometer (Cu Kα radiation – 1.5406 Å, 40 kV, 30 mA). The GIXD pattern was collected in the range 20° < 2θ < 80°, scan speed of 3° min^{-1}, with an incident angle, θ = 8°.

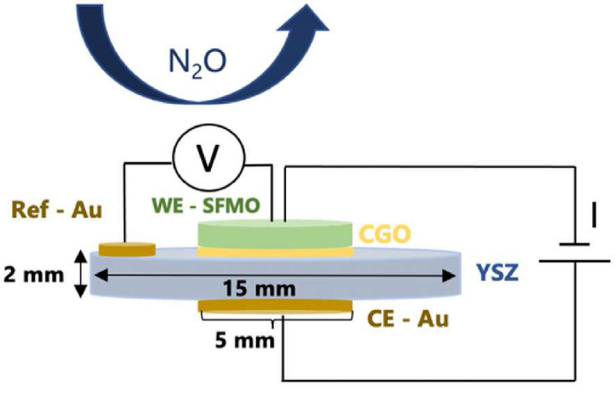


Fig. 1 – Schematic representation of developed 3-probe cell.

Electrochemical impedance spectroscopy (EIS)

Electrochemical Impedance Spectroscopy (EIS) was used to retrieve the electrochemical characteristics of the SFMO||CGO||YSZ||Au 3-probe cell, using an Electrochemie Autolab PGSTAT302 N analyzer. Measurements were executed in the 650–850 °C range in the direction of decreasing temperature, in N_2O and in air atmospheres. The EIS data was collected in a frequency range between 0.01 Hz and 100 kHz with signal amplitude 50 mV. Equilibrium conditions were ensured by using dwell times of 1 h before impedance measurements at each temperature, followed by repeated measurements after a further hour under identical conditions.

Electrocatalytic tests

The potentiostat/galvanostat Autolab PGSTAT302 N analyzer was also used to apply a constant electrical current to the 3-probe electrochemical cell. The N_2O used in this work has a purity of >99.5% with N_2 < 0.4%. To monitor alterations in the gas phase composition during polarization, an 8YSZ oxygen sensor was placed near the 3-probe cell sample and used to quantify the oxygen partial pressure using a procedure described in our previous article [29]. The measurements were performed at 600 °C, 700 °C and 800 °C at open circuit conditions (OCV) and in galvanostatic mode (*i.e.*, −0.25 A and −0.1 A of applied current). A thermocouple was used near the sample aiming to monitor temperature variations.

Results and discussion

Structural, microstructural, and thermal characterization

Different crystalline structures have been reported for the SFMO material with the unit cell structure of the Sr–Fe–Mo–O system being very susceptible to the synthesis conditions, due to its influence on the oxygen content. As such, various crystalline structures have been suggested at room temperature by different authors, including cubic $Fm\bar{3}m$ and $Pm\bar{3}m$, tetragonal, *I4/mcm*, and *I4/mmm*, and orthorhombic, *Pnma*. Table 1 summarizes these different structures and the respective synthesis method of these authors.

Fig. 2 shows the X-ray diffraction (XRD) patterns of the SFMO cathode, synthesized in our work, obtained from the sol-gel method after calcination temperature of 1200 °C. The *Rietveld* refined (experimental, calculated and difference) patterns for the obtained powder, are shown in Fig. 2a, where a pure SFMO phase was achieved. The patterns were indexed to a cubic symmetry ($Fm\bar{3}m$ space group), in good agreement with literature, where similar synthesis methods allowed SFMO to be obtained in this cubic symmetry [14,32,34]. The lattice parameters obtained from *Rietveld* refinement are shown in Table 2. The low R_{wp} factor value of 3.93% indicates the high quality of the pattern fitting.

Afterward, we performed thermogravimetric analysis (TG) to measure the lattice oxygen loss promoted by the reduction

Table 1 – Synthesis method used to obtain pure phase of $Sr_2Fe_{1.5}Mo_{0.5}O_{6-\delta}$.

Synthesis method	Synthesis conditions	Crystallite structure	Lattice parameters/Å	Ref
Mixtures of $SrCO_3$, Fe_2O_3, $Fe_2(MoO_4)_3$	1000 °C, 12 °C min^{-1}, dwell time of 12 h, quickly cooling, followed by 5 h at 1200 °C, during 12 h in air repeated 10 times with intermittent re-grinding of the sample	*I4/mcm*	$a = 5.5548$ $c = 7.8783$	[23]
Microwave-assisted combustion method:	1000 °C, 3 °C min^{-1} for 5 h in air	$Fm\bar{3}m$	$a = 7.8447$	[14]
Citrate route	1100 °C, 5 h in air	$Pm\bar{3}m$	a =3.9271	[30]
One-step combustion method	1050 °C, 5 h in air	*Pnma*	$a = 3.9124$ $b = 3.9033$ $c = 3.9146$	[31]
Combustion method	1000 °C, 12 h in air	$Fm\bar{3}m$	$a = 7.8664$	[32]
Solid-state of $Sr(NO_3)_2$, Fe_2O_3 MoO_3	1100 °C, 10 h in air	$Pm\bar{3}m$	$a = 3.9203$	[33]
Combustion method	1100 °C, 10 h in air	$Fm\bar{3}m$	$a = 7.8388$	[34]
Sol-gel combustion	1100 °C, 5 h in air	*Cmmm*	$a = 7.8300$	[35]
Sol-gel combustion method	1100 °C, 5 h in air	$Pm\bar{3}m$	$a = 3.9196$	[36]

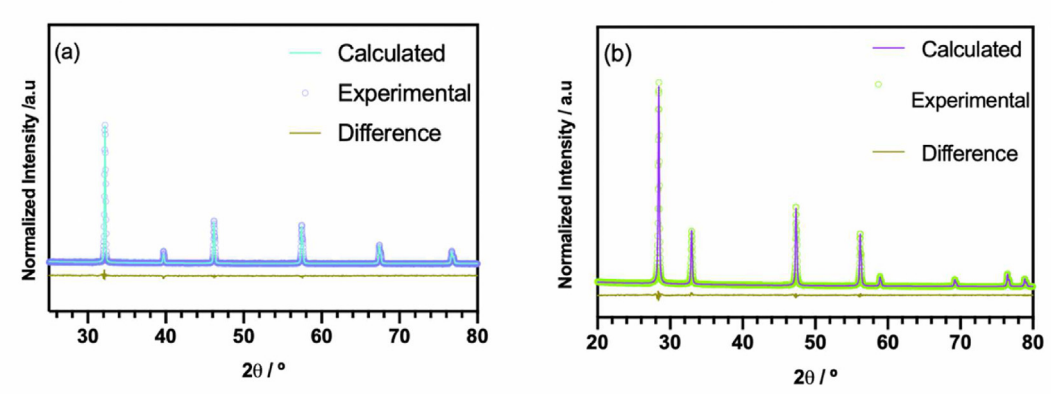


Fig. 2 – XRD pattern with *Rietveld* refinement analysis of (a) SFMO cathode obtained under air atmosphere after calcination at 1200 °C and (b) CGO synthesized by combustion method.

Table 2 – *Rietveld* refinement extracted parameters of SFMO and CGO10.

$Sr_2Fe_{1.5}Mo_{0.5}O_{6-\delta}$	
Space group	$Fm\bar{3}m$ (Cubic symmetry)
Lattice parameter (a= b = and c)/Å	7.8384 (2)
Phase angle (a = b = g)/°	90
R_{wp}/%	3.93
S	1.4497
χ^2	2.1015
$Ce_{0.9}Gd_{0.1}O_{2-\delta}$	
Space group	$Fm\bar{3}m$ (Cubic)
Lattice parameter (a= b = and c)/Å	5.4190 (4)
Phase angle (a = b = g)/°	90
R_{wp}/%	4.62
S	1.47
χ^2	2.1609

of metal ions during heating in dry air. As shown in Fig. 3, SFMO shows a mass loss of 2%, associated oxygen loss and subsequent creation of oxygen vacancies, as observed in a previous work [36,37]. The sample was analyzed by XRD after TGA, and the XRD patterns before and after the tests are shown in Fig. 4. The XRD is observed to be very similar to the as-synthesized material, maintaining the cubic structure of space group $Fm\bar{3}m$. Nonetheless, the lattice parameters retrieved from the *Rietveld* analysis, shown in Table 3, reveal a small increase in lattice parameter due to metal ions reduction (Mo^{5+}/Mo^{6+} and Fe^{3+}/Fe^{4+} pairs), resulting in a small peak shift toward lower 2θ angles (Fig. 4b). This reduction reaction can lead to the creation of oxygen vacancies, according to:

$$O_O^{\times} + 2Fe_{Fe}^{\times} = 2Fe_{Fe}' + \frac{1}{2}O_2(g) + V_O^{\bullet\bullet} \quad (1)$$

$$O_O^{\times} + 2Mo_{Mo}^{\times} = 2Mo_{Mo}' + \frac{1}{2}O_2(g) + V_O^{\bullet\bullet} \quad (2)$$

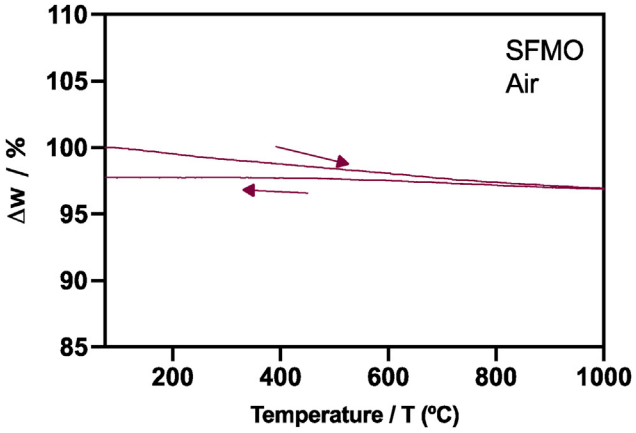


Fig. 3 – Thermogravimetry (TG) of SFMO in air.

Table 3 – Lattice parameters of as synthesized and after TGA.

Space group	as synthesized	after TGA in air
	$Fm\bar{3}m$ (Cubic symmetry)	$Fm\bar{3}m$ (Cubic symmetry)
Lattice parameter ($a = b =$ and c)/Å	7.8384 (2)	7.8559 (7)
Phase angle ($a = b = g$)/°	90	90
R_{wp}/%	3.93	3.47
S	1.4497	1.0866
χ^2	2.1015	1.1807

where $O_O^{\times}$ denotes an oxygen ion on the regular lattice site, $V_O^{\bullet\bullet}$ a negatively double charged oxygen vacancy, $2Fe_{Fe}^{\times}$ represents a Fe ion on the regular site and $2Fe'_{Fe}$ denotes a negative charge defect of Fe with respect to the lattice (with a similar nomenclature for Mo).

The cross-section of the developed 3-probe cell was observed by Scanning Electron Microscopy (SEM) coupled with Energy Dispersive Spectroscopy (EDS). As seen Fig. 4a, the SFMO electrode film shows a porous microstructure, which is suitable for gas diffusion [27,38–40], exhibiting a thickness of around 43 μm. Meanwhile, the CGO buffer layer presents a thickness of 5.7 μm, being well adhered to the YSZ substrate and the SFMO electrode, Fig. 4a. The corresponding EDS map, Fig. 5b shows that the CGO buffer layer successfully prevents a direct contact between the SFMO electrode and the YSZ electrolyte, as previously suggested to be essential to avoid potential chemical inter-reaction [41].

Electrochemical impedance spectroscopy (EIS) analysis

Fig. 6a depicts the impedance arcs obtained from the SFMO||CGO||YSZ||Au 3-probe cells at 800 °C in N_2O and air atmospheres. While there are substantial changes in the magnitude of the impedance data, an interesting feature is that the spectra (Fig. 6a) denote a similar number of at least two or more contributions in both conditions. In this respect, the high-frequency semicircle is relatively constant, while the middle- and the low-frequency parts of the spectra change dramatically with atmosphere. In both cases, the spectra were modeled with a resistor (R) (an ohmic contribution that was removed for better visualization) in series with two $R||CPE$ arranged in parallel (here, CPE represents a constant phase element), followed by a *Gerischer* element to represent the low-frequency contribution. The resultant fitting curve is also depicted in Fig. 6a, where we can see a very good match with the experimental data. The total polarization resistance (R_p) was here calculated by including all these contributions ($R_p = R_{HF} + R_{MF} + R_{LF}$).

The temperature dependence of R_p, in both N_2O and air atmospheres, is depicted in Fig. 6b. As observed, R_p present a higher resistance value in N_2O atmosphere at low temperatures, whereas they tend to converge with increasing temperature. This interesting observation requires a detailed analysis on each of these processes.

From the EIS data (Fig. 6a), the first non-ohmic contribution appearing at high-frequency ($R_{HF}||CPE_{HF}$) presents a very low capacitance value, ~10^{-7} F cm^{-2}, which lies between the typical values observed for the electrolyte (grain boundary) processes, *i.e.*, ≤10^{-8} F cm^{-2} and those for the electrode-electrolyte interfacial transfer processes, *i.e.*, $10^{-6} - 10^{-5}$ F cm^{-2} [42]. Therefore,

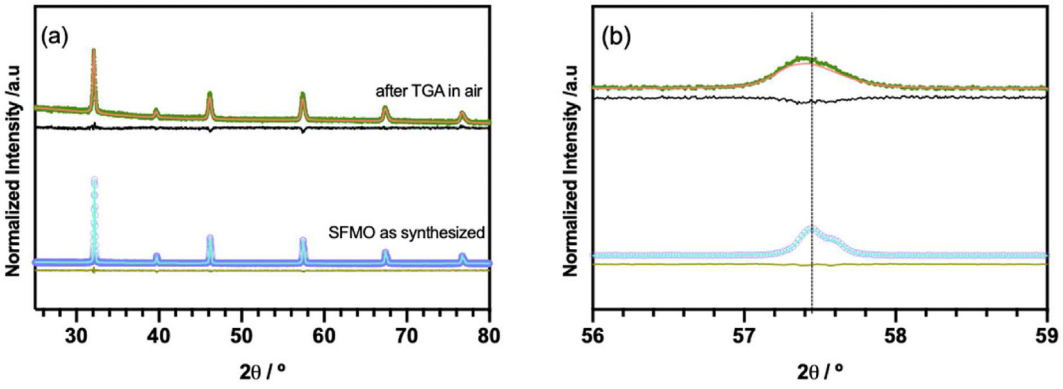


Fig. 4 – XRD pattern of SFMO as synthesized and after TGA in air. (b) XRD patterns represented from 56° to 59° 2θ, showing the shift in the peak position.

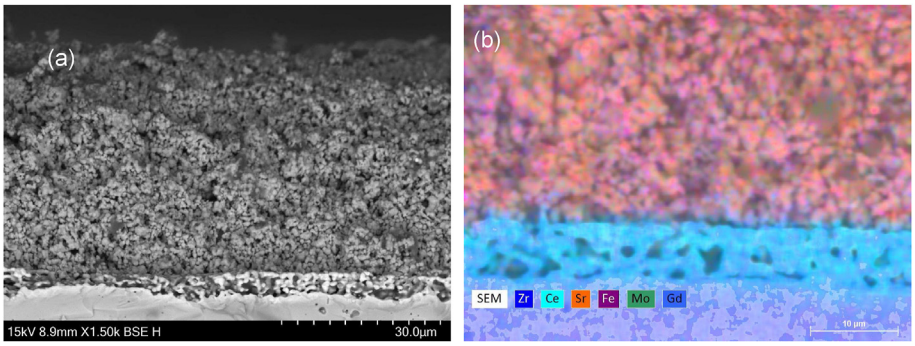


Fig. 5 – a) Cross-section image obtained by Scanning Electron Microscopy (SEM) for the SFMO||CGO||YSZ||Au 3-probe cell; b-i) Energy Dispersive Spectroscopy (EDS) elemental map.

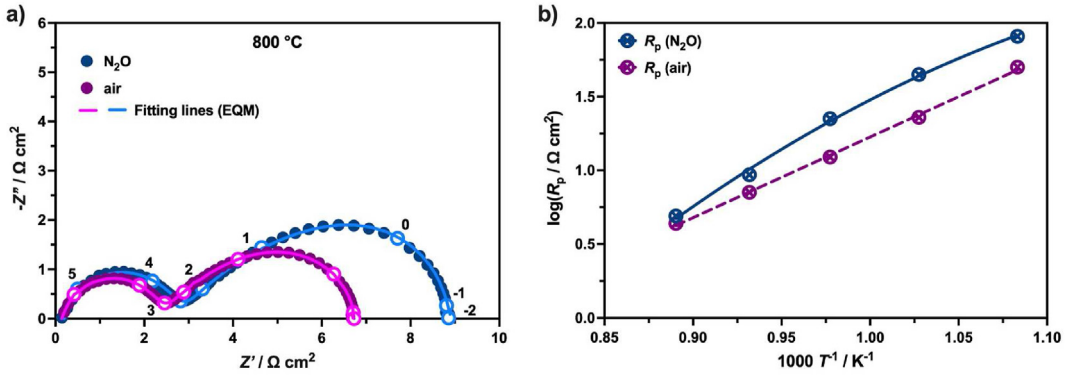


Fig. 6 – a) Impedance arcs obtained from the SFMO||CGO||YSZ||Au 3-probe cells (the numbers indicate the decades of the measuring frequencies). The data was obtained at 800 °C in air and N_2O atmospheres and the ohmic resistance was removed for better visualization; b) temperature dependence of the total polarization (R_p) in both air and N_2O atmospheres.

such feature may be indicative of a very fast process, possibly attributed to the oxygen-transfer occurring at the YSZ||CGO interface,

$$V_O^{\bullet\bullet}(CGO) + O_O^x(YSZ) \rightarrow V_O^{\bullet\bullet}(YSZ) + O_O^x(CGO) \quad (3)$$

The magnitude of R_{HF} was also found to gain increasing importance in N_2O atmosphere with decreasing temperature (Fig. 7a), in comparison with the behavior in air, with an estimated activation energy (E_a) value of 0.85 eV ± 0.02 eV in air (Table 4). Conversely, the second contribution, $R_{MF}||CPE_{MF}$,

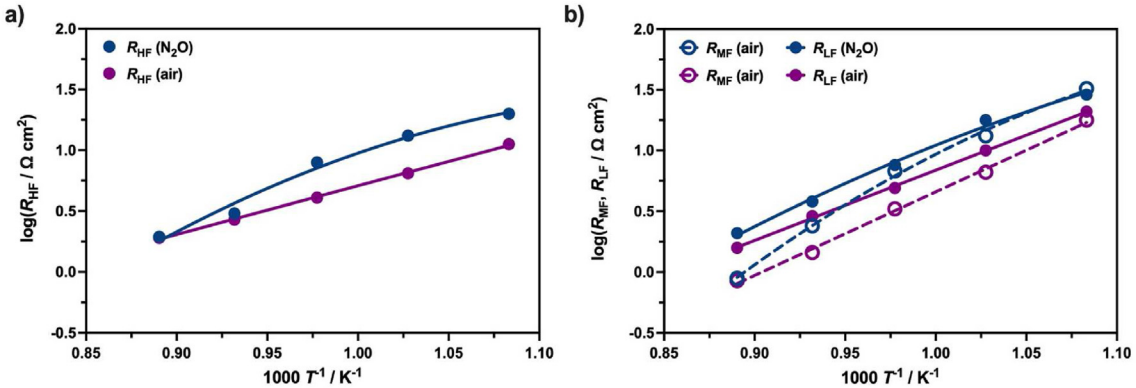


Fig. 7 – Temperature dependence of a) the high-frequency (R_{HF}); b) the middle-frequency (R_{MF}) and the low-frequency (R_{LF}) polarization resistances. Data obtained in air and N_2O atmospheres in the temperature range 650–850 °C.

Table 4 – Activation energy (E_a) values determined in air for the different electrochemical terms.

Atmosphere	R_p	R_{HF}	R_{MF}	R_{LF}	Y_0	K_a
Air (650–850 °C)	1.14 ± 0.03	0.85 ± 0.02	1.40 ± 0.08	1.19 ± 0.03	0.32 ± 0.03	1.82 ± 0.02

occurring at intermediate-frequency, presents a power factor (n) ~ 0.5 that is indicative of a diffusion-related response [43], possibly at the SFMO||CGO interface,

$$V_O^{\bullet\bullet}(SFMO) + O_O^x(CGO) \rightarrow V_O^{\bullet\bullet}(CGO) + O_O^x(SFMO) \quad (4)$$

The increasing importance in N_2O atmosphere was also observed in R_{MF}, as seen in Fig. 7b, presenting the highest E_a value of 1.40 eV ± 0.08 eV in air, among all polarization resistances (Table 4).

This noted atmosphere dependency of both R_{HF} and R_{MF} terms and may indicate that the availability of O^{2-} species to diffuse through both interfaces is significantly lower in N_2O at lower temperatures, as it will become clearer in the following discussions.

Finally, the low-frequency contribution, $R_{LF}||Q_{LF}$, has the shape of a *Gerischer*-like dispersion. Such a feature is characteristic of a reaction (capacitive part) coupled with diffusion, which is typically found in the literature of mixed ionic electronic conductors (MIECs) [43–46]. In this regard, the low frequency part of the *Gerischer* impedance can be related to the surface-related electrode processes, which typically include adsorption, reduction, and exchange steps [43–46]. The *Gerischer* resistance can be calculated using the following equation, where the K_a-Gerischer and the Y_0-Gerischer parameters are related to the oxygen-ion diffusion and the oxygen surface exchange, respectively:

$$R_G = \frac{1}{Y_0\sqrt{K_a}} \quad (5)$$

From Fig. 8, we can clearly observe that the $R_{LF}||CPE_{LF}$ process is dominated by the Y_0-parameter, which includes information related to the oxygen self-diffusion coefficient (D^*), as explained previously. In this respect, a striking feature was found in the case of the Y_0-parameter, which presents a relatively low E_a value of 0.32 eV ± 0.03 eV in air (Table 4). This points towards a preferential diffusion path through the bulk of the SFMO electrode, as a likely result of the high oxygen self-diffusion coefficient of the SFMO material, D^* ~10^{-7} cm^2 s^{-1} at 800 °C [47]. This was also observed in the work of Rolle et al. [48], using composite oxygen electrodes based on calcium cobaltites and CGO, where the authors noted a decrease in the E_a for the Y_0-parameter in the case of the sample with increased fraction of ionic-conducting phase (CGO). Therefore, it would be expected a more temperature dependent Y_0-parameter on a predominant surface diffusion scenario. For example, this is the case found for other MIECs presenting a surface-preferential diffusion path, *e.g.*, the calcium cobaltites [43,49], with a much lower D^* ~10^{-10} cm^2 s^{-1} [50], for which a much higher E_a value of the Y_0-parameter (0.89 eV) was reported [40].

In contrast, a higher E_a value of 1.82 ± 0.02 eV was found in this work for the K_a-parameter. This parameter includes information related to the surface-exchange properties of the SFMO material, *i.e.*, the surface exchange coefficient (K^*). In this respect, the following equation represents the mechanism involved with an oxygen ion at the reaction site ($O^-_{reaction\ site}$) that is incorporated in an oxygen-ion vacancy ($V_O^{\bullet\bullet}$) [36]:

$$O^-_{reaction\ site}(SFMO) + V_O^{\bullet\bullet}(SFMO) + e^-(SFMO) \rightarrow O_O^x(CGO) \quad (6)$$

where $O^-_{reaction\ site}$ is a negatively charged monoatomic oxygen species at the electrode reaction site, $V_O^{\bullet\bullet}$ is an oxygen-ion vacancy, e^-, an electron coming from the current collector and O_O^x, an oxygen incorporated in the lattice. In this regard, as seen in Fig. 6a, the $R_{LF}||CPE_{LF}$ process has a significant contribution to the overall electrode impedance. Fig. 7b depicts the temperature dependence of R_G obtained for the SFMO||CGO||YSZ||Au 3-probe cell in both N_2O and air atmospheres, showing that this term presents a higher magnitude in N_2O atmospheres at low temperatures, while converging slightly with increasing temperature. At first sight, this observation may be in line with the expected convergence of the measured

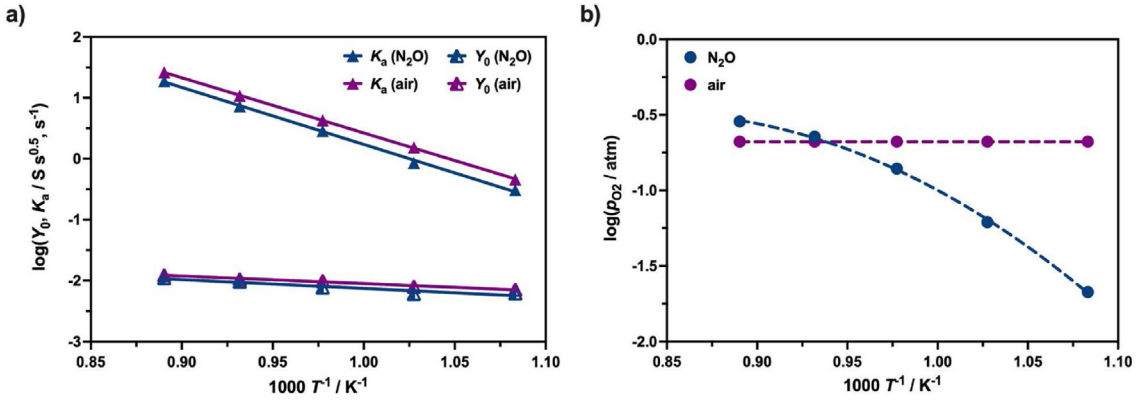


Fig. 8 – Temperature dependence of a) the Y_0-parameter and the K_a-parameter; b) the oxygen partial pressure (p_{O2}). Data obtained in air and N_2O atmospheres in the temperature range 650–850 °C.

p_{O2} with temperature for the N_2O and air atmospheres (Fig. 7b). In this regard, evolution of the p_{O2} of the N_2O atmosphere is observed to be strong with temperature, rapidly increasing with increasing temperature, until the p_{O2} of the air atmosphere is met at a temperature of around 800 °C. Such behavior may suggest that the p_{O2} will play an important role in the impedance response, being, significantly dependent on the N_2O conversion and, therefore, temperature.

Nonetheless, for $T \geq 800$ °C, the measured p_{O2} in N_2O is notably higher when compared to the air atmosphere, approaching that expected for complete N_2O conversion ($p_{O2} = 0.33$ atm). Despite this factor, the magnitude of R_{LF} is shown to be always lower in air than in the N_2O atmosphere (Fig. 7b). As such, the electrocatalytic properties of the SFMO cathode cannot directly be related to simple p_{O2} variations. In the light of these observations, we may suggest competition between direct N_2O reduction and that of gaseous O_2, which arises from thermal conversion, on the surface of the SFMO electrode. In other words, the amount of oxygen available for incorporation, $O^-_{\text{reaction site}}$, may be that obtained by direct chemisorption and electrochemical reduction of O_2 or N_2O species present in the gas phase, with that of N_2O giving the slightly higher polarization resistance.

Electrocatalytic tests

The above-described typical cathode processes that take place at charge-transfer electrodes obey the Faraday's law, *i.e.*, the current is obtained due to the reduction of oxygen-related species occurring at the gas-electrode interface. Conversely, in the non-Faradaic case, these charged species do not cross the interface, and the current is carried out by the charging of the electrical double layer (battery like behavior). This situation can be more precisely described as [51]:

$$O^{2-}(YSZ + CGO) \rightarrow [O^{\delta-} - \delta^{+}](SFMO) + 2e^{-}(SFMO) \quad (7)$$

where $[O^{\delta-} - \delta^{+}](SFMO)$ represents the ionic adsorbed oxygen-related species at the gas-electrode interface. Nonetheless, this interface can be still directly related to the characteristics of the *Gerischer* impedance that has been previously adopted to describe this phenomenon [51].

To test the electrochemical conversion in real conditions, the conversion of N_2O was determined using a simple YSZ oxygen sensor, in which we determined the p_{O2} values, assuming the following equilibrium:

$$N_2O(g) \rightarrow \frac{1}{2}O_2(g) + N_2(g) \quad (8)$$

The electrochemical reduction of N_2O using SFMO as an electrocatalyst was studied at 600, 700 and 800 °C under applied galvanostatic transients (*i.e.*, −0.10 A and −0.25 A) (Fig. 9a). It is clearly visible that a significant increase of the catalytic rate is observed due to the electrochemical pumping of O^{2-} from the SFMO through the YSZ electrolyte. Consequently, the N_2O conversion follows the same trend, increasing as more O^{2-} is electrochemically pumped due to the applied current (Fig. 9b). In the current work the observed enhanced conversion was noted to be completely reversible over time, with the cell running for 5 days in total. This reversible behavior was observed, in all tested conditions over this timeframe.

Fig. 10a shows the conversion increment $\left(\frac{C_f}{C_i}\right)$, where C_f and C_i are the initial and final conversions, evidencing that in all tested conditions there is an electrochemical promotion. Particularly, at 600 °C when the current increases, the increment factor increases as well, from 2.64 to 5.01, with this effect being more pronounced at low temperatures. This can be related to the fact that at lower temperatures the unpromoted conversion is also lower (~1.2% for 50 mL min^{-1}, Fig. 9c, resulting in a more valuable effect of the applied polarization [29]). Conversely, at 700 °C, the maximum conversion increment factor was only 1.31 @ −0.25 A and at 800 °C 1.12 @ −0.25 A, as expected due to the lower N_2O unpromoted conversions at higher temperatures (~16% and ~60% at 700 °C and 800 °C, respectively, for 50 mL min^{-1}, Fig. 9c). In addition, the conversion increment is also equivalent to the enhancement ratio $\left(\rho = \frac{r}{r_0}\right)$. In this regard, systems exhibiting a non-electrochemical modification of catalytic activity (NEMCA) effect are characterized by a $\rho \neq 1$). Fig. 10a, the conversion increment is always higher than unity, thus, indicating a NEMCA effect.

The Faradaic Efficiency was also calculated using the following expression:

$$|\Lambda| = \frac{\Delta r}{I/nF} = \frac{\text{change in catalytic rate}}{\text{removal of } O^{2-} \text{ from the catalyst}} \quad (9)$$

where $\Delta r = r - r_0$ is the change in the catalytic rate due to the polarization (mol s^{-1}), r is the electropromoted catalytic rate under polarization (mol s^{-1}), r_0 is the catalytic rate under OCV (mol s^{-1}), I is the applied current (A), n is the number of transferred electrons, and F is the Faraday constant (C mol^{-1}).

The values of the Faradaic Efficiency are shown in Fig. 10b, and, in all tested conditions, this value exceeds unity, evidencing the electrochemical promotion due to an non-faradaic process [52]. At 600 °C, the value of $|\Lambda|$ increases with increasing conversion increment factor, achieving the highest $|\Lambda|$ value of 3.94 when a current of −0.25 A was applied. Similar non-Faradaic electrochemical behavior is observed when the temperature increases to 700 and 800 °C. Nonetheless, the magnitude of this effect is diminished, with lower values of $|\Lambda|$ obtained, with increasing temperature. Such results highlight that the benefit of the electrochemical promotion is much more pronounced when the catalytic (unpromoted) conversion is poor (*i.e.*, at lower temperatures, Fig. 9 (c)).

Although the existent literature on cathodes in N_2O fuel using 3-probe cells is scarce, it is interesting to compare the performance of the developed SFMO cathode with previous works obtained in other similar conditions, such as in NO_x environment. For example, Hwang et al. [53] studied the electrochemical reduction of NO using $LaCO_3$ perovskite from 600 °C to 800 °C, applying voltages above 2 V. In such conditions, a reduction up to 40% of NO was obtained, nevertheless, the authors observed that the current efficiency was lower than 1.5%, decreasing with increasing temperature, in good agreement with our results. Another example, is our previous work [29], where $La_{0.6}Sr_{0.4}Co_{0.2}Fe_{0.8}O_{3-\delta}$ (LSCF) was studied in N_2O environment at 600–800 °C, showing a comparable performance with our developed SFMO cathode.

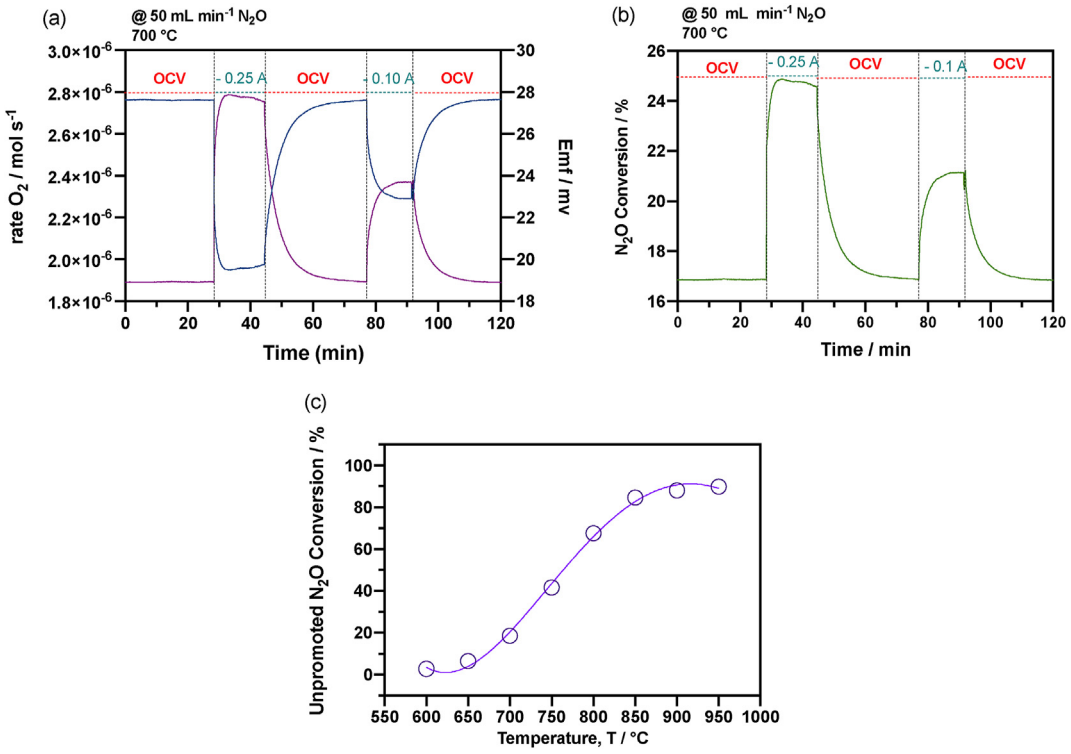


Fig. 9 – a) Typical example of an applied galvanostatic transient at 700 °C on the 3-probe cell setup: a) catalytic rate and *Emf* and b) N_2O conversion. c) The N_2O unpromoted conversion is also shown for comparison. Measurements taken @50 mL min^{-1}.

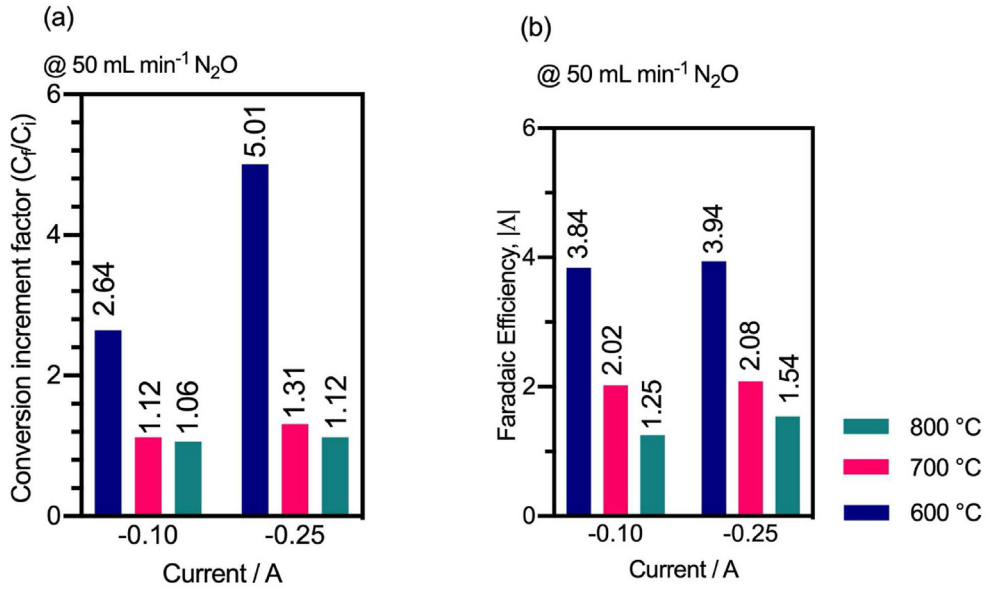


Fig. 10 – (a) Conversion increment and (b) Faradaic efficiency ($|\Lambda|$) *vs.* current at 600 °C, 700 °C and 800 °C.

Post-mortem analysis

The surface of the developed electrochemical cell was analyzed after the NEMCA experiments by X-ray grazing incidence measurements (GIXD) studies to observe if there was any degradation due to the electrochemical tests. Fig. 11 shows the XRD patterns obtained for different incident grazing angles. As can be seen, all the peaks were indexed to pure

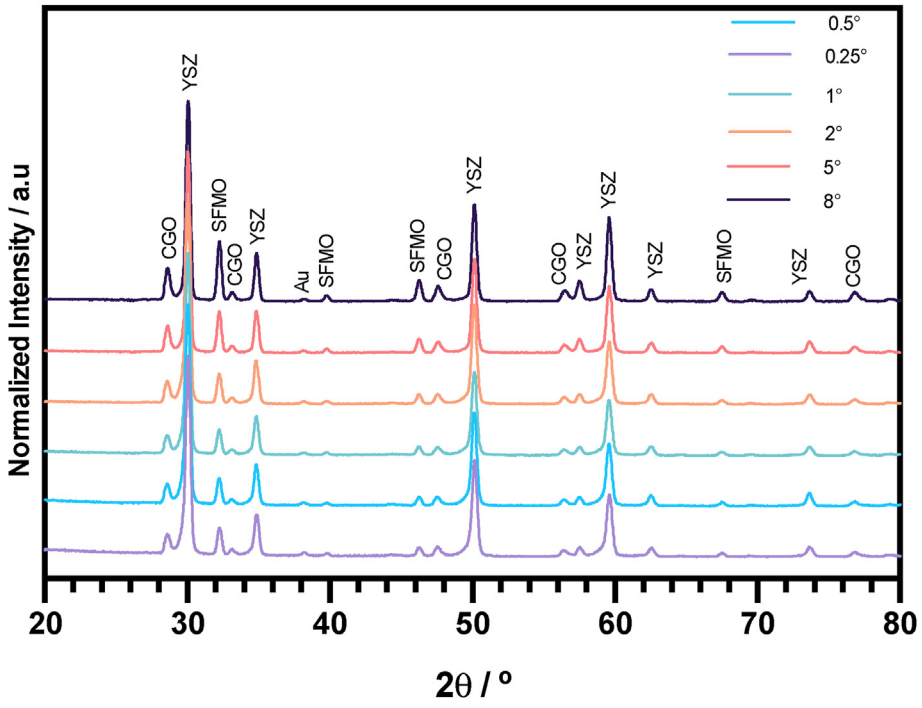


Fig. 11 – *Post-mortem* grazing incidence X-ray diffraction (GIXD) analysis with different incident angles (0.25, 0.5, 1, 2, 5 and 8°) of the developed electrochemical cell.

phase of SFMO, CGO and YSZ, with no evidence of phase degradation and inter-reaction. A small peak around 38.20° was indexed to Au, which was the reference electrode used in this work.

Conclusions

SFMO electrocatalyst powder was successfully synthesized by a sol-gel method followed by calcination in air at 1200 °C, crystallizing in a cubic symmetry ($Fm\bar{3}m$ space group). Phase stability was confirmed by thermogravimetric analysis (TG) in air up to 1000 °C, which revealed only a small weigh loss of 2%, likely associated in the oxygen loss and subsequent creation of oxygen vacancies. The cross-section microstructure (SEM) of the developed electrochemical cell revealed a well-formed assembly, while EDS mapping highlights distinct layers, where the CGO buffer layer successfully prevents direct contact and chemical inter-reaction between the SFMO electrode and the YSZ electrolyte.

EIS was successfully used to characterize the electrochemical characteristics of the SFMO electrode in both N_2O and air atmospheres. Data were analyzed by an equivalent circuit including a *Gerischer* element (R_{LF}), which was used to describe the main electrode process including surface reaction coupled with diffusion. This analysis allowed to underscore that the electroreduction mechanism on the SFMO cathode possibly involves a competition between both O_2 and N_2O species, due to exhibiting differing p_{O2} dependences of the R_G term as a function of temperature.

The electrocatalytic performance of the SFMO electrode was assessed by applied galvanostatic transients between 600 °C and 800 °C. Under the maximum applied current (−0.25 A), the highest Faradaic efficiency was observed ($|\Lambda|$) at lower temperatures (600 °C). In contrast, at higher temperatures, $|\Lambda|$ was found to be significantly lower, a behavior that was ascribed to the higher unpromoted conversion under these temperatures. However, in all cases, $|\Lambda| > 1$, which was an indication of a NEMCA effect, being also corroborated by a conversion increment > 1. These results demonstrate the viability of SFMO electrodes as promising electrocatalysts for N_2O reduction, as well as providing detailed insights on the correlation between the electrode impedance and the N_2O electroreduction mechanism.

Declaration of Competing Interest

The authors declare that they have no known competing financial interests or personal relationships that could have appeared to influence the work reported in this paper.

Acknowledgements

Laura I. V. Holz, Vanessa C. D. Graça and Celina Fernandes acknowledge for Fundação para a Ciência e a Tecnologia the PhD grant PD/BDE/142837/2018, SFRH/BD/130218/2017 and 2021.07014.BD, respectively. Francisco J. A. Loureiro is thankful for the Investigator Grant CEECIND/02797/2020. The authors also acknowledge the projects, PTDC/CTM-CTM/2156/2020, 2022.02498.PTDC, 2022.09319.PTDC, PTDC/QUI-ELT/3681/2020, POCI-01-0247-FEDER-039926, UIDB/00481/2020 and UIDP/00481/2020 from FCT, and CENTRO-01-0145-FEDER-

181241 and CENTRO-01-0145-FEDER-022083 from Centro Portugal Regional Operational Programme (Centro2020), under the PORTUGAL 2020 Partnership Agreement, through the European Regional Development Fund.). This work was financially supported by LA/P/0045/2020 (ALiCE), UIDB/00511/2020 and UIDP/00511/2020 (LEPABE), funded by national funds through FCT/MCTES (PIDDAC).

REFERENCES

[1] Tian H, Chen G, Lu C, Xu X, Ren W, Zhang B, et al. Global methane and nitrous oxide emissions from terrestrial ecosystems due to multiple environmental changes. Ecosys Health Sustain 2015;1:1–20. https://doi.org/10.1890/EHS14-0015.1.

[2] van den Brink RW, Booneveld S, Pels JR, Bakker DF, Verhaak MJF. Catalytic removal of N_2O in model flue gases of a nitric acid plant using a promoted Fe zeolite. Appl Catal B Environ 2001;32:73–81. https://doi.org/10.1016/S0926-3373(00)00294-0.

[3] Davidson EA. The contribution of manure and fertilizer nitrogen to atmospheric nitrous oxide since 1860. Nat Geosci 2009;2:659–62. https://doi.org/10.1038/ngeo608.

[4] Syakila A, Kroeze C. The global nitrous oxide budget revisited. Greenh Gas Meas Manag 2011;1:17–26. https://doi.org/10.3763/ghgmm.2010.0007.

[5] Richardson D, Felgate H, Watmough N, Thomson A, Baggs E. Mitigating release of the potent greenhouse gas N_2O from the nitrogen cycle - could enzymic regulation hold the key? Trends Biotechnol 2009;27:388–97. https://doi.org/10.1016/j.tibtech.2009.03.009.

[6] Frutos OD, Quijano G, Aizpuru A, Muñoz R. A state-of-the-art review on nitrous oxide control from waste treatment and industrial sources. Biotechnol Adv 2018;36:1025–37. https://doi.org/10.1016/j.biotechadv.2018.03.004.

[7] Rees RM, Baddeley JA, Bhogal A, Ball BC, Chadwick DR, Macleod M, et al. Nitrous oxide mitigation in UK agriculture. Soil Sci Plant Nutr 2013;59:3–15. https://doi.org/10.1080/00380768.2012.733869.

[8] Alves L, Holz LIV, Fernandes C, Ribeirinha P, Mendes D, Fagg DP, et al. A comprehensive review of NO_x and N_2O mitigation from industrial streams. Renew Sustain Energy Rev 2021;155:111916. https://doi.org/10.1016/j.rser.2021.111916.

[9] Li T, Rabuni MF, Kleiminger L, Wang B, Kelsall GH, Hartley UW, et al. A highly-robust solid oxide fuel cell (SOFC): simultaneous greenhouse gas treatment and clean energy generation. Energy Environ Sci 2016;9:3682–6. https://doi.org/10.1039/c6ee02562e.

[10] Deng H, Feng C, Zhang W, Mi Y, Wang X, Dong W, et al. The electrolyte-layer free fuel cell using a semiconductor-ionic $Sr_2Fe_{1.5}Mo_{0.5}O_6$ - $Ce_{0.8}Sm_{0.2}O_2$ composite functional membrane. Int J Hydrogen Energy 2017;42:25001–7. https://doi.org/10.1016/j.ijhydene.2017.08.113.

[11] Liu Q, Yang C, Dong X, Chen F. Perovskite $Sr_2Fe_{1.5}Mo_{0.5}O_{6-\delta}$ as electrode materials for symmetrical solid oxide electrolysis cells. Int J Hydrogen Energy 2010;35:10039–44. https://doi.org/10.1016/j.ijhydene.2010.08.016.

[12] Osinkin DA. Precursor of $Pr_2NiO_{4+\delta}$ as a highly effective catalyst for the simultaneous promotion of oxygen reduction and hydrogen oxidation reactions in solid oxide electrochemical devices. Int J Hydrogen Energy 2021;46:24546–54. https://doi.org/10.1016/j.ijhydene.2021.05.022.

[13] Liu Q, Bugaris DE, Xiao G, Chmara M, Ma S, Zur Loye HC, et al. $Sr_2Fe_{1.5}Mo_{0.5}O_{6-\delta}$ as a regenerative anode for solid oxide fuel cells. J Power Sources 2011;196:9148–53. https://doi.org/10.1016/j.jpowsour.2011.06.085.

[14] Liu Q, Dong X, Xiao G, Zhao F, Chen F. A novel electrode material for symmetrical SOFCs. Adv Mater 2010;22:5478–82. https://doi.org/10.1002/adma.201001044.

[15] Osinkin DA. Kinetics of CO oxidation and redox cycling of $Sr_2Fe_{1.5}Mo_{0.5}O_6$ electrode for symmetrical solid state electrochemical devices. J Power Sources 2019;418:17–23. https://doi.org/10.1016/j.jpowsour.2019.02.026.

[16] Osinkin DA, Beresnev SM, Bogdanovich NM. Influence of Pr_6O_{11} on oxygen electroreduction kinetics and electrochemical performance of $Sr_2Fe_{1.5}Mo_{0.5}O_{6-\delta}$ based cathode. J Power Sources 2018;392:41–7. https://doi.org/10.1016/j.jpowsour.2018.04.076.

[17] Muñoz-García AB, Pavone M, Ritzmann AM, Carter EA. Oxide ion transport in $Sr_2Fe_{1.5}Mo_{0.5}O_{6-\delta}$, a mixed ion-electron conductor: new insights from first principles modeling. Phys Chem Chem Phys 2013;15:6250–9. https://doi.org/10.1039/C3CP50995H.

[18] Xu C, Zhen S, Ren R, Chen H, Song W, Wang Z, et al. Cu-Doped $Sr_2Fe_{1.5}Mo_{0.5}O_{6-\delta}$ as a highly active cathode for solid oxide electrolytic cells. Chem Commun 2019;55:8009–12. https://doi.org/10.1039/C9CC03455B.

[19] Bouwmeester HJM, Den Otter MW, Boukamp BA. Oxygen transport in $La_{0.6}Sr_{0.4}Co_{1-y}Fe_yO_{3-\delta}$. J Solid State Electrochem 2004;8:599–605. https://doi.org/10.1007/s10008-003-0488-3.

[20] Liu Q, Yang C, Dong X, Chen F. Perovskite $Sr_2Fe_{1.5}Mo_{0.5}O_{6-\delta}$ as electrode materials for symmetrical solid oxide electrolysis cells. Int J Hydrogen Energy 2010;35:10039–44. https://doi.org/10.1016/j.ijhydene.2010.08.016.

[21] Li Y, Chen X, Yang Y, Jiang Y, Xia C. Mixed-conductor $Sr_2Fe_{1.5}Mo_{0.5}O_{6-\delta}$ as robust fuel electrode for pure CO_2 reduction in solid oxide electrolysis cell. ACS Sustainable Chem Eng 2017;5:11403–12. https://doi.org/10.1021/acssuschemeng.7b02511.

[22] Goodenough JB, Huang YH. Alternative anode materials for solid oxide fuel cells. J Power Sources 2007;173:1–10. https://doi.org/10.1016/j.jpowsour.2007.08.011.

[23] Bugaris DE, Hodges JP, Huq A, Chance WM, Heyden A, Chen F, et al. Investigation of the high-temperature redox chemistry of $Sr_2Fe_{1.5}Mo_{0.5}O_{6-\delta}$ via in situ neutron diffraction. J Mater Chem 2014;2:4045–54. https://doi.org/10.1039/c3ta14913g.

[24] Pan X, Wang Z, He B, Wang S, Wu X, Xia C. Effect of Co doping on the electrochemical properties of $Sr_2Fe_{1.5}Mo_{0.5}O_6$ electrode for solid oxide fuel cell. Int J Hydrogen Energy 2013;38:4108–15. https://doi.org/10.1016/j.ijhydene.2013.01.121.

[25] Sun W, Li P, Xu C, Dong L, Qiao J, Wang Z, et al. Investigation of Sc doped $Sr_2Fe_{1.5}Mo_{0.5}O_6$ as a cathode material for intermediate temperature solid oxide fuel cells. J Power Sources 2017;343:237–45. https://doi.org/10.1016/j.jpowsour.2017.01.063.

[26] Gao J, Meng X, Luo T, Wu H, Zhan Z. Symmetrical solid oxide fuel cells fabricated by phase inversion tape casting with impregnated $SrFe_{0.75}Mo_{0.25}O_{3-\delta}$ (SFMO) electrodes. Int J Hydrogen Energy 2017;42:18499–503. https://doi.org/10.1016/j.ijhydene.2017.03.205.

[27] Loureiro FJA, Yang T, Stroppa DG, Fagg DP. $Pr_2O_2SO_4$–$La_{0.6}Sr_{0.4}Co_{0.2}Fe_{0.8}O_{3-\delta}$: a new category of composite cathode for intermediate temperature-solid oxide fuel cells. J Mater Chem 2015;3:12636–41. https://doi.org/10.1039/c4ta06640e.

[28] Loureiro FJA, Macedo DA, Nascimento RM, Cesário MR, Grilo JPF, Yaremchenko AA, et al. Cathodic polarisation of composite LSCF-SDC IT-SOFC electrode synthesised by

one-step microwave self-assisted combustion. J Eur Ceram Soc 2019;39:1846–53. https://doi.org/10.1016/j.jeurceramsoc.2019.01.013.
[29] Holz LIV, Graça VCD. The electrochemical promotion of nitrous oxide reduction on a lanthanum strontium iron cobalt cathode. Int J Energy Res 2022:1–11. https://doi.org/10.1002/er.8213.
[30] Osinkin DA, Lobachevskaya NI, Suntsov AY. The electrochemical behavior of the promising $Sr_2Fe_{1.5}Mo_{0.5}O_{6-\delta}$ + $Ce_{0.8}Sm_{0.2}O_{1.9-\delta}$ anode for the intermediate temperature solid oxide fuel cells. J Alloys Compd 2017;708:451–5. https://doi.org/10.1016/j.jallcom.2017.03.057.
[31] Hou M, Sun W, Li P, Feng J, Yang G, Qiao J, et al. Investigation into the effect of molybdenum-site substitution on the performance of $Sr_2Fe_{1.5}Mo_{0.5}O_{6-\delta}$ for intermediate temperature solid oxide fuel cells. J Power Sources 2014;272:759–65. https://doi.org/10.1016/j.jpowsour.2014.09.043.
[32] Fan Y, Xi X, Li J, Wang Q, Xiang K, Medvedev D, et al. Barium-doped $Sr_2Fe_{1.5}Mo_{0.5}O_{6-\delta}$ perovskite anode materials for protonic ceramic fuel cells for ethane conversion. J Am Ceram Soc 2022;105:3613–24. https://doi.org/10.1111/jace.18329.
[33] Porotnikova NM, Ananyev MV, Osinkin DA, Khodimchuk AV, Fetisov AV, Farlenkov AS, et al. Increase in the density of $Sr_2Fe_{1.5}Mo_{0.5}O_{6-\delta}$ membranes through an excess of iron oxide: the effect of iron oxide on transport and kinetic parameters. Surface Interfac 2022;29:101784. https://doi.org/10.1016/j.surfin.2022.101784.
[34] Xi X, Liu J, Luo W, Fan Y, Zhang J, Luo JL, et al. Unraveling the enhanced kinetics of $Sr_2Fe_{1+x}Mo_{1-x}O_{6-\delta}$ electrocatalysts for high-performance solid oxide cells. Adv Energy Mater 2021;11:1–10. https://doi.org/10.1002/aenm.202102845.
[35] Zhang L, Sun W, Xu C, Ren R, Yang X, Qiao J, et al. Attenuating a metal-oxygen bond of a double perovskite oxide: via anion doping to enhance its catalytic activity for the oxygen reduction reaction. J Mater Chem 2020;8:14091–8. https://doi.org/10.1039/d0ta04820h.
[36] Ren R, Wang Z, Xingguang M, Wang X, Chunming X, Qiao J, et al. Tailoring the oxygen vacancy to achieve fast intrinsic proton transport in a perovskite cathode for protonic ceramic fuel cells. Appl Energy Mater 2020;3:4914–22.
[37] Gou M, Ren R, Sun W, Xu C, Meng X, Wang Z, et al. Nb-doped $Sr_2Fe_{1.5}Mo_{0.5}O_{6-\delta}$ electrode with enhanced stability and electrochemical performance for symmetrical solid oxide fuel cells. Ceram Int 2019;45:15696–704. https://doi.org/10.1016/j.ceramint.2019.03.130.
[38] Fulgêncio EBGA, Loureiro FJA, Melo KPV, Silva RM, Fagg DP, Campos LFA, et al. Boosting the oxygen reduction reaction of the misfit $[Ca_2CoO_{3-\delta}]_q[CoO_2]$ (C349) by the addition of praseodymium oxide. J Alloys Compd 2019;788:148–54. https://doi.org/10.1016/j.jallcom.2019.02.209.
[39] Loureiro FJA, Souza GS, Graça VCD, Araújo AJM, Grilo PF, Macedo DA, et al. Nickel-copper based anodes for solid oxide fuel cells running on hydrogen and biogas: study using ceria-based electrolytes with electronic short-circuiting correction. J Power Sources 2019;438:227041–9. https://doi.org/10.1016/j.jpowsour.2019.227041.
[40] Araújo AJM, Loureiro FJA, Holz LIV, Grilo JPF, Macedo DA, Paskocimas CA, et al. Composite of calcium cobaltite with praseodymium-doped ceria: a promising new oxygen electrode for solid oxide cells. Int J Hydrogen Energy 2021. https://doi.org/10.1016/j.ijhydene.2021.06.049.
[41] Dos Santos-Gómez L, León-Reina L, Porras-Vázquez JM, Losilla ER, Marrero-López D. Chemical stability and compatibility of double perovskite anode materials for SOFCs. Solid State Ionics 2013;239:1–7. https://doi.org/10.1016/j.ssi.2013.03.005.
[42] Irvine JTS, Sinclair DC, West AR. Electroceramics: characterization by impedance spectroscopy. Adv Mater 1990;2:132–8. https://doi.org/10.1002/adma.19900020304.
[43] Araújo AJM, Loureiro FJA, Holz LIV, Graça VCD, Grilo JPF, Macedo DA, et al. Creating new surface-exchange pathways on the misfit Ca-cobaltite electrode by the addition of an active interlayer. J Power Sources 2021;510:230417. https://doi.org/10.1016/j.jpowsour.2021.230417.
[44] Loureiro FJA, Araújo AJM, Paskocimas CA, Macedo DA, Fagg DP. Polarisation mechanism of the misfit Ca-cobaltite electrode for reversible solid oxide cells. Electrochim Acta 2021;373:137928. https://doi.org/10.1016/j.electacta.2021.137928.
[45] Hildenbrand N, Nammensma P, Blank DHA, Bouwmeester HJM, Boukamp BA. Influence of configuration and microstructure on performance of $La_2NiO_{4+\delta}$ intermediate-temperature solid oxide fuel cells cathodes. J Power Sources 2013;238:442–53. https://doi.org/10.1016/j.jpowsour.2013.03.192.
[46] Adler SB, Lane JA, Steele BCH. Electrode kinetics of porous mixed-conducting oxygen electrodes. J Electrochem Soc 1996;143:3554–64. https://doi.org/10.1149/1.1837252.
[47] Osinkin DA, Khodimchuk AV, Porotnikova NM, Bogdanovich NM, Fetisov AV, Ananyev MV. Rate-determining steps of oxygen surface exchange kinetics on $Sr_2Fe_{1.5}Mo_{0.5}O_{6-\delta}$. Energies 2020;13. https://doi.org/10.3390/en13010250.
[48] Rolle A, Mohamed HAA, Huo D, Capoen E, Mentré O, Vannier R-N, et al. $Ca_3Co_4O_{9+\delta}$, a growing potential SOFC cathode material: impact of the layer composition and thickness on the electrochemical properties. Solid State Ionics 2016;294:21–30. https://doi.org/10.1016/J.SSI.2016.06.001.
[49] Boukamp BA, Rolle A, Vannier RN, Sharma RK, Djurado E. Electrostatic spray deposited $Ca_3Co_4O_{9+\delta}$ and $Ca_3Co_4O_{9+\delta}$/$Ce_{0.9}Gd_{0.1}O_{1.95}$ cathodes for SOFC: a comparative impedance analysis study. Electrochim Acta 2020;362:137142. https://doi.org/10.1016/j.electacta.2020.137142.
[50] Thoreton V, Hu Y, Pirovano C, Capoen E, Nuns N, Mamede AS, et al. Oxygen transport kinetics of the misfit layered oxide $Ca_3Co_4O_{9+\delta}$. J Mater Chem 2014;2:19717–25. https://doi.org/10.1039/C4TA02198C.
[51] Brosda S, Badas T, Vayenas CG. Study of the mechanism of the electrochemical promotion of Rh/YSZ catalysts for C_2H_4 oxidation via AC impedance spectroscopy. Top Catal 2011;54:708. https://doi.org/10.1007/s11244-011-9679-9.
[52] Vayenas CG. Bridging electrochemistry and heterogeneous catalysis. J Solid State Electrochem 2011;15:1425–35. https://doi.org/10.1007/s10008-011-1336-5.
[53] Hwang HJ, Awano M. Preparation of $LaCoO_3$ catalytic thin film by the sol-gel process and its NO decomposition characteristics. J Eur Ceram Soc 2001;21:2103–7. https://doi.org/10.1016/S0955-2219(01)00181-9.